

Dust Motion and Possibility of Dust Growth in a Growing Circumstellar Disk

Shunta Koga^{1*} and Masahiro N. Machida^{1†}

¹*Department of Earth and Planetary Sciences, Faculty of Sciences, Kyushu University, Fukuoka 819-0395, Japan*

30 November 2022

ABSTRACT

We calculate the evolution of a star-forming cloud core using a three-dimensional resistive magnetohydrodynamics simulation, treating dust grains as Lagrangian particles, to investigate the dust motion in the early star formation stage. We prepare six different-sized set of dust particles in the range $a_d = 0.01\text{--}1000\ \mu\text{m}$, where a_d is the dust grain size. In a gravitationally collapsing cloud, a circumstellar disk forms around a protostar and drives a protostellar outflow. Almost all the small dust grains ($a_d \lesssim 10\text{--}100\ \mu\text{m}$) initially distributed in the region $\theta_0 \lesssim 45^\circ$ are ejected from the center by the outflow, where θ_0 is the initial zenith angle relative to the rotation axis, whereas only a small number of the large dust grains ($a_d \gtrsim 100\ \mu\text{m}$) distributed in the region are ejected. All other grains fall onto either the protostar or disk without being ejected by the outflow. Regardless of the dust grain size, the behavior of the dust motion is divided into two trends after dust particles settle into the circumstellar disk. The dust grains reaching the inner disk region from the upper envelope preferentially fall onto the protostar, while those reaching the outer disk region or disk outer edge from the envelope can survive without an inward radial drift. These surviving grains can induce dust growth. Thus, we expect that the outer disk regions could be a favored place of planet formation.

Key words: stars: formation – stars: magnetic field – MHD – ISM: dust, , extinction– ISM: jets and outflows

1 INTRODUCTION

Many planetary systems have been confirmed since 1995 (Mayor & Queloz 1995). Planets form in disks around young stars (Benisty et al. 2021), as shown in recent ALMA observations of the formation sites of planets (e.g. ALMA Partnership et al. 2015). Ring and gap structures

* E-mail: kshunta3403@gmail.com

† E-mail: machida.masahiro.018@m.kyushu-u.ac.jp

can be clearly seen in protoplanetary disks observed by dust thermal emission ([Andrews et al. 2018](#)), and these structures are likely to be related to planet formation ([Andrews 2020](#)). It is considered that dust grains aggregate and grow to form planets in the disks around young stars ([Hayashi et al. 1985](#)). However, it is very difficult to observe the disks in the very early phase during which planet formation begins. Therefore, we cannot confidently identify when and how dust grows and planet formation begins in a disk based only on observations.

Theoretical studies can help us to understand dust growth and planet formation (e.g. [Blum & Wurm 2008](#)). In such studies, planet formation (or dust growth) is conventionally considered to begin in an isolated and relatively low-mass disk after the gas accretion onto the disk ends. Such a disk is called the minimum mass solar nebula (MMSN, [Hayashi et al. 1985](#)) and is observed around Class II young stellar objects. However, recent observations have confirmed signs of planet formation in very young growing circumstellar disks around Class 0 and I protostars ([Sheehan et al. 2020](#); [Tychoniec et al. 2020](#); [Podio et al. 2020](#)), implying that planet formation begins earlier than previously thought.

The formation and evolution of disks around young stars have been theoretically investigated in the framework of star formation (e.g. [Machida & Matsumoto 2011](#)). Physical quantities such as the mass and radius of the disk vary over time in the star formation process ([Tsukamoto et al. 2020](#); [Xu & Kunz 2021a](#); [Lee et al. 2021](#)). Thus, it is not sufficient to consider the MMSN to be the initial condition of planet formation. It is appropriate to consider the dust growth and planet formation from the beginning of the disk formation epoch in the star formation process.

The star formation process has been investigated with three-dimensional magneto hydrodynamics (MHD) simulations, in which only the gas dynamics are calculated and the dust motion is not explicitly considered ([Machida et al. 2004](#); [Banerjee & Pudritz 2006](#); [Hennebelle & Fromang 2008](#); [Tomida et al. 2013](#); [Machida et al. 2014](#); [Tsukamoto et al. 2015](#); [Xu & Kunz 2021b](#)). However, it is important to consider the behavior of dust grains in the star formation process to investigate the dust growth and planet formation, because dust is a fundamental element of planet formation. There are a few studies calculating the dust motion in three-dimensional MHD star-formation simulations ([Lebreuilly et al. 2020](#); [Tsukamoto et al. 2021b](#); [Koga et al. 2022](#)). [Lebreuilly et al. \(2020\)](#) performed a star formation simulation with the inclusion of dust and detailed the increase and decrease of dust around the circumstellar disk (see also [Tsukamoto et al. 2021a](#)). [Tsukamoto et al. \(2021b\)](#) also calculated the star formation process including dust and showed that the dust grains are

swept by the protostellar outflow and that part of the swept dust falls onto the disk. They considered the dust growth or dust size evolution with single-sized approximation. It should be noted that, recently, the dust growth in the star formation process were also investigated with various (or different) approaches in [Marchand et al. \(2022, 2021\)](#), [Bate \(2022\)](#) and [Tu et al. \(2022\)](#).

Our calculation settings are approximately similar to [Lebreuilly et al. \(2020\)](#) and [Tsukamoto et al. \(2021b\)](#). Our previous study ([Koga et al. 2022](#), hereafter Paper I) showed almost the same results as in [Lebreuilly et al. \(2020\)](#) and [Tsukamoto et al. \(2021b\)](#), but used a novel method in which the behavior of the dust grains is calculated using a Lagrangian formulation and the fluid motion is calculated using an Eulerian formulation. Following Paper I, this study focuses on the behavior of dust in both a gravitationally collapsing cloud and a circumstellar disk, starting the simulation from the prestellar stage (or the molecular cloud core). Our study differs from the past studies of [Lebreuilly et al. \(2020\)](#) and [Tsukamoto et al. \(2021b\)](#) in the treatment of dust, in that while past studies adopted a fluid approximation, our study treats the dust particles as Lagrange particles, calculated separately from the gas component (for detail, see Paper I). Using this treatment, we can individually trace the motion of each dust particle and investigate the behavior of dust in the disk during the early star formation stage. As described above, the implementation of an MHD nested grid code in the treatment of the dust was presented in Paper I, in which we also presented the trajectories of dust in the infalling envelope focusing on the coupling between the gas and dust. In this paper, we mainly present the motion of dust in the circumstellar disk.

The structure of this paper is as follows. The numerical settings and methods are described in §2 and the calculation results are presented in §3. We discuss dust motion, dust growth and planet formation in the early star formation stage in §4. A summary is presented in §5.

2 NUMERICAL METHOD AND SETTINGS

The numerical method and settings are the same as in Paper I and we only briefly explain them here (for details, see §2 and Appendix of Paper I).

As the initial state, a gas sphere with a critical Bonner–Ebert density profile is adopted. The mass and radius of the initial cloud are $M_{\text{cl}} = 1.25 M_{\odot}$ and $R_{\text{cl}} = 6.13 \times 10^3 \text{ au}$, respectively. A rigid rotation ($\Omega_0 = 2 \times 10^{-13} \text{ s}^{-1}$) is added to the initial cloud and a uniform magnetic field ($B_0 = 5.1 \times 10^{-5} \text{ G}$) is imposed over the whole computation domain. The

Table 1. Initial spatial distributions of dust particles

Coordinate	Initial particle locations
r_0	10–6130 au (every 10 au, 613 locations)
ϕ_0	$0^\circ, 90^\circ, 180^\circ, 270^\circ$ (every 90° , 4 locations)
θ_0	$0^\circ, 15^\circ, 30^\circ, 45^\circ, 60^\circ, 75^\circ, 90^\circ$ (every 15° , 7 locations)

Table 2. Dust grain sizes used in the calculation

Dust grain size a_d [μm]
0.01, 0.1, 1, 10, 100, 1000

mass-to-flux ratio normalized by the critical value $(2\pi G^{1/2})^{-1}$ is $\mu = 3$. The initial state is the same as that in [Tomida et al. \(2017\)](#) and [Aso & Machida \(2020\)](#).

In the simulation, the MHD part is calculated by our three-dimensional non-ideal MHD nested grid code ([Machida et al. 2004, 2006, 2009](#); [Machida & Hosokawa 2013](#)). The spatial resolution and generation criterion of the grid are described in Paper I. The cell width and grid size of the finest grid are 0.374 au and 24 au, respectively, while those of the coarsest grid are 3.07×10^3 au and 1.96×10^5 au. The number of cells in each grid is $(i, j, k) = (64, 64, 64)$. Five levels of grid are prepared before the calculation, while 14 levels of grid are nested just before protostar formation (for details, see Paper I). In the simulation, a sink of radius $r_{\text{sink}} = 1$ au is created after the density exceeds $n_{\text{thr}} = 10^{13} \text{ cm}^{-3}$ ([Machida et al. 2014, 2016](#)). In addition, dust particles are implemented as super-particles, for which the feedback from the dust to the gas is ignored, as described in Paper I. It should be noted that we assume that the dust particles do not interact with each other.

We include a total of 102,984 dust particles in the simulation. The initial spatial distribution of the particles is shown in Table 1, in spherical coordinates. As described in the table, the dust locations are distributed every 10 au in the range 10–6130 au in the radial direction r_0 , every 90° in the azimuthal direction ϕ_0 , and every 15° in the zenith direction θ_0 . We prepare six different grain sizes (or six different-size set of grains) in the range $a_d = 0.01\text{--}1000 \mu\text{m}$, listed in Table 2, where a_d is the radius of a dust grain. The settings for the distribution of dust particles adopted in this study are identical to those in Paper I.

3 RESULTS

3.1 Time sequence of gas density and velocity distributions

Before presenting the dust motion results, we will describe the gas evolution. Since the dust grains are coupled with the gas to some degree, it is important to examine the gas evolution from a Eulerian perspective.

Fig. 1 plots the density and velocity distributions of the gas at four different epochs. An elliptical structure, which corresponds to the first core supported by both thermal pressure and rotation, can be seen just before protostar formation (top right panel of Fig. 1). After protostar formation, the central region shrinks (right panels of Fig. 1) and a rotationally supported disk appears (left panels of Fig. 1). Since gas accretion onto the disk continues during the simulation, the disk increases in size with time. The simulation was stopped at $t = 85000$ yr after the cloud collapse begins. At the end of the simulation, the protostellar mass (or sink mass) is $M_{\text{ps}} = 0.0784 M_{\odot}$, which is 6.3 % of the initial cloud mass. At this epoch, the disk has a radius of about ~ 20 au (bottom left panel of Fig. 1).

Fig. 2 shows the density and velocity distributions at the same epoch as in the bottom panels of Fig. 1, though note that the spatial scales of Fig. 1 (~ 50 au) and Fig. 2 (~ 1500 au) are very different. Fig. 2 indicates that the protostellar outflow is driven near the center of the cloud. At the end of the calculation, the size of the outflow exceeds ~ 1000 au. As described below, a portion of the dust grains is ejected from the central region or disk by the outflow (see Paper I).

3.2 Motion of dust particles

3.2.1 Dust motion from envelope to disk

As described in §3.1, the gas evolution is obtained from a Eulerian simulation while the dust grains are calculated as Lagrange particles. Thus, we can trace the trajectory of each dust particle with the gas evolution. In this subsection, we show the dependence of the dust orbital evolution on their initial positions.

Figs. 3 and 4 show the time evolution of the distance from the central protostar (or sink), $r = \sqrt{x^2 + y^2 + z^2}$, for dust grains with sizes of $a_d = 0.01 \mu\text{m}$ (Fig. 3) and $1000 \mu\text{m}$ (Fig. 4), respectively. In each panel, the initial zenith angle of the dust particles ($\theta_0 = 0, 15, 30, 45, 60, 75,$ and 90°) is fixed.

Firstly, we describe the evolution of dust particles with a size of $a_d = 0.01 \mu\text{m}$ (Fig. 3). In

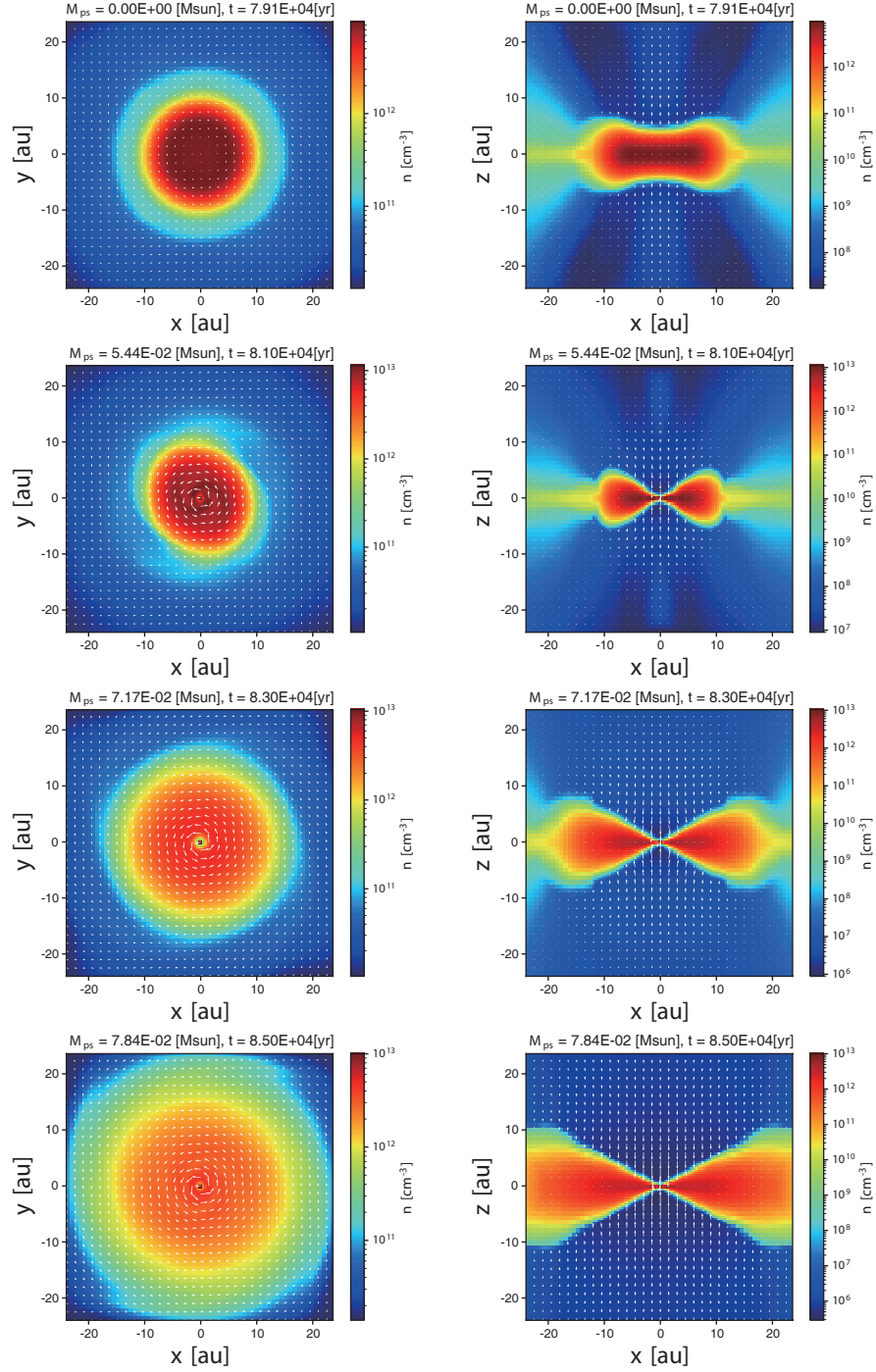


Figure 1. Gas density (color) and velocity (arrows) distributions on the $z = 0$ (left) and $y = 0$ (right) planes at four different epochs. The protostellar mass (or sink mass) and elapsed time are listed above each panel.

Fig. 3, we plot the evolution of dust particles having different initial radial positions in the range $r_0 = 1000\text{--}2450$ au. All the dust particles that initially have $\theta = 0^\circ$ reach the sink by $t = 79.3$ kyr (Fig. 3a). These particles fall toward the center (or sink) due to the gravity of the central protostar, even though the gas pressure gradient somewhat retards their infall.

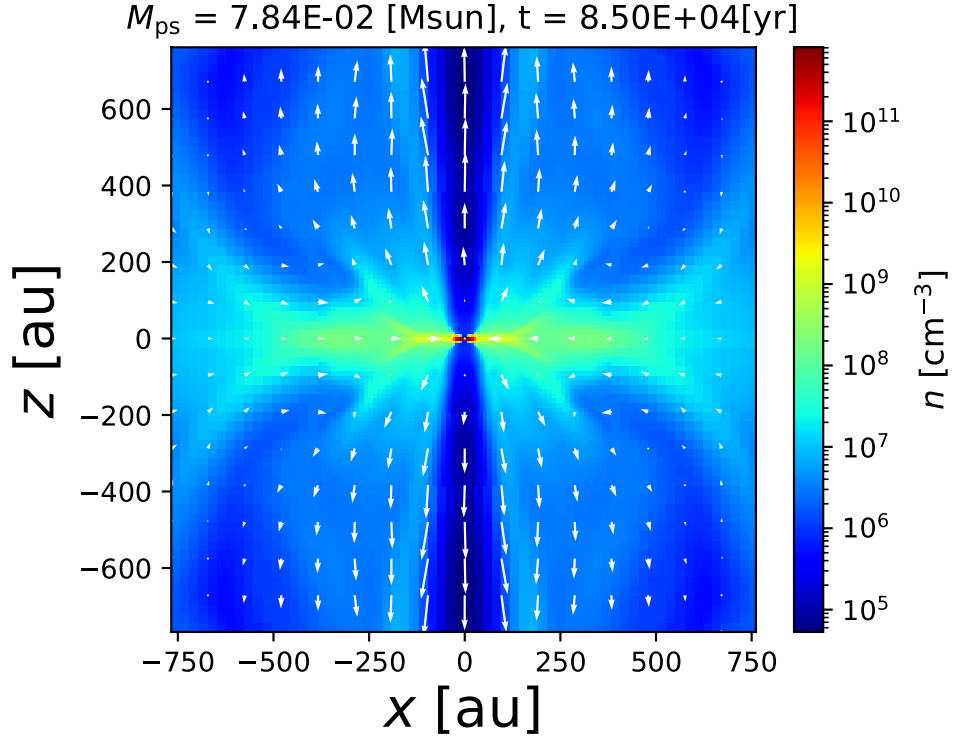


Figure 2. Gas density (color) and velocity (arrows) distributions on the $y = 0$ plane. The protostellar mass and the elapsed time after the cloud collapse begins are given above the plot.

In addition, the dust particles plotted in Fig. 3a are not swept up by the outflow because they have fallen onto the sink before the outflow appears.

The distance evolution for dust particles with $\theta_0 = 15^\circ$ clearly exhibits two trends depending on the initial radius, as seen in Fig. 3b. Dust particles with an initial radius smaller than $r_0 \lesssim 1900$ au fall onto the disk (gray line) within $t < 79.5$ kyr. They then orbit within the disk and finally fall onto the sink by $t \simeq 80$ kyr. Note that the gray line in each panel corresponds to the radius of the rotationally supported disk. The identification prescription of the disk is described in Paper I and §3.3. Note also that we confirmed that the particles are located within the disk when the distance of each particle is smaller than the disk radius (or gray line). On the other hand, all the dust particles having an initial radius larger than $r_0 \gtrsim 1900$ au increase their distances from the center with time, indicating that they are outflowing from the center with the gas (see Fig. 2).

For dust particles with $\theta_0 = 30^\circ$ (Fig. 3c), the distance for the particles with an initial radius larger than $r_0 \gtrsim 1500$ au begins to increase after initially decreasing, indicating that these particles are trapped and entrained by the gas outflow while falling toward the center. Thus, they fall toward the center at an early stage and outflow from the center at a later stage. The other particles having an initial radius smaller than $r_0 < 1500$ au orbit within

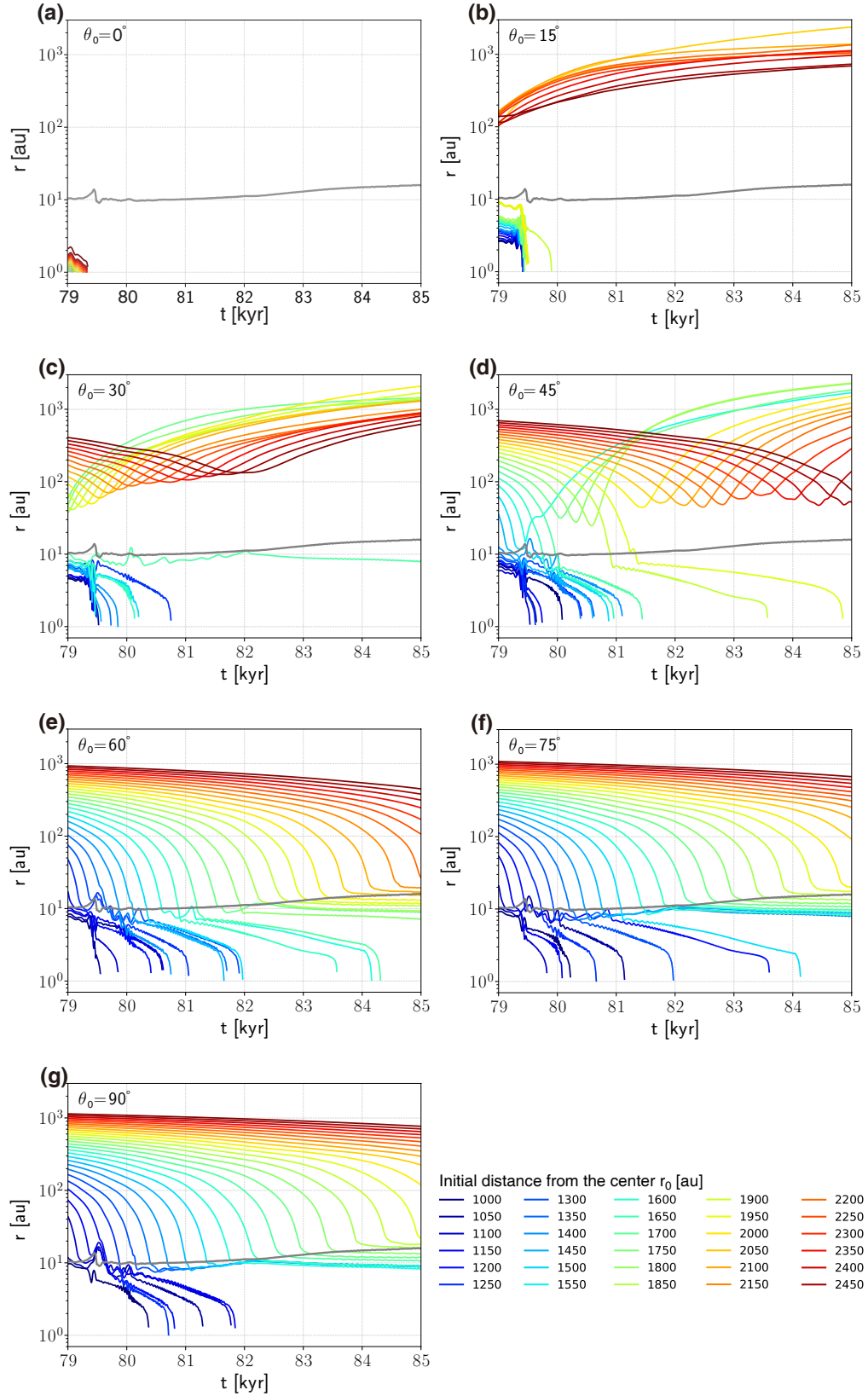


Figure 3. Distance of dust particles from the center against the elapsed time after the cloud collapse begins. Each panel shows the distance of dust with $\theta_0 = 0, 15, 30, 45, 60, 75, 90^\circ$ (from left top to right bottom). The dust grain size is $a_d = 0.01 \mu\text{m}$. The initial distances from the center in units of au for each particle are indicated by color, as given on the bottom right. The disk size against the elapsed time is also plotted in gray in each panel.

the disk and fall onto the protostar, except for one particle plotted in Fig. 3c with an initial radius $r_0 = 1650$ au, which survives without falling to the center. This surviving particle orbits within the disk while maintaining a distance of ~ 10 au after $t > 79$ kyr. In addition, this survivor does not immediately fall to the equatorial plane, but rotates 10 times in the range $0 < z < 3$ au within the hydrostatic equilibrium region of the gas disk before it reaches the equatorial plane of the disk (for details, see below).

A similar trend can be confirmed for the dust particles with $\theta_0 = 45^\circ$ (Fig. 3d). The particles initially placed far from the center eventually outflow from the center, while those initially placed near the center fall onto the sink after they enter into the disk region. On the other hand, we confirm that particles at $r_0 = 1850$ and 1900 au continue to fall into the center after they are momentarily rolled up by the outflow. Even when the particles are initially placed at almost the same region, their final fates are somewhat different. The outflow launching region varies with time, and the timing of the dust particles reaching the disk surface is influenced by whether they are swept up by the outflow.

For the dust particles with $\theta_0 \geq 60^\circ$ (Fig. 3e–g), we see no rapid increase in the distance from the center, indicating that the particles plotted in these panels are not captured by the outflow. After the dust particles initially located near the center ($r_0 \lesssim 1500$ au) reach the disk, they orbit in the disk while gradually falling to the center, as seen in Fig. 3e–g. On the other hand, the particles initially located far from the center ($r_0 \gtrsim 1800$ au) orbit within the disk without falling onto the protostar by the end of the simulation. After these particles reach the disk, they orbit in the disk while maintaining a distance of ~ 10 –20 au. The distances from the center for these surviving particles are comparable to and slightly smaller than the disk radius. Thus, these particles orbit around the outer disk region by the end of the simulation. Although the protostar and disk gradually evolve, these particles continue to orbit in the disk maintaining almost the same radii. As a result, among the dust particles with $\theta_0 \gtrsim 60^\circ$, there are many survivors orbiting in the disk outer region for a long time.

Next, we describe the behavior of the dust grains with a size of $a_d = 1000 \mu\text{m}$ shown in Fig. 4. Note that the initial distances of the particles from the center are different from Fig. 3. We plotted only the dust particles initially placed in the range $r_0 = 2000$ –3450 au, because most of the dust particles having initially small radii ($r_0 \lesssim 2000$ au) fell directly onto the sink without passing through the circumstellar disk (Paper I). Similar to the case

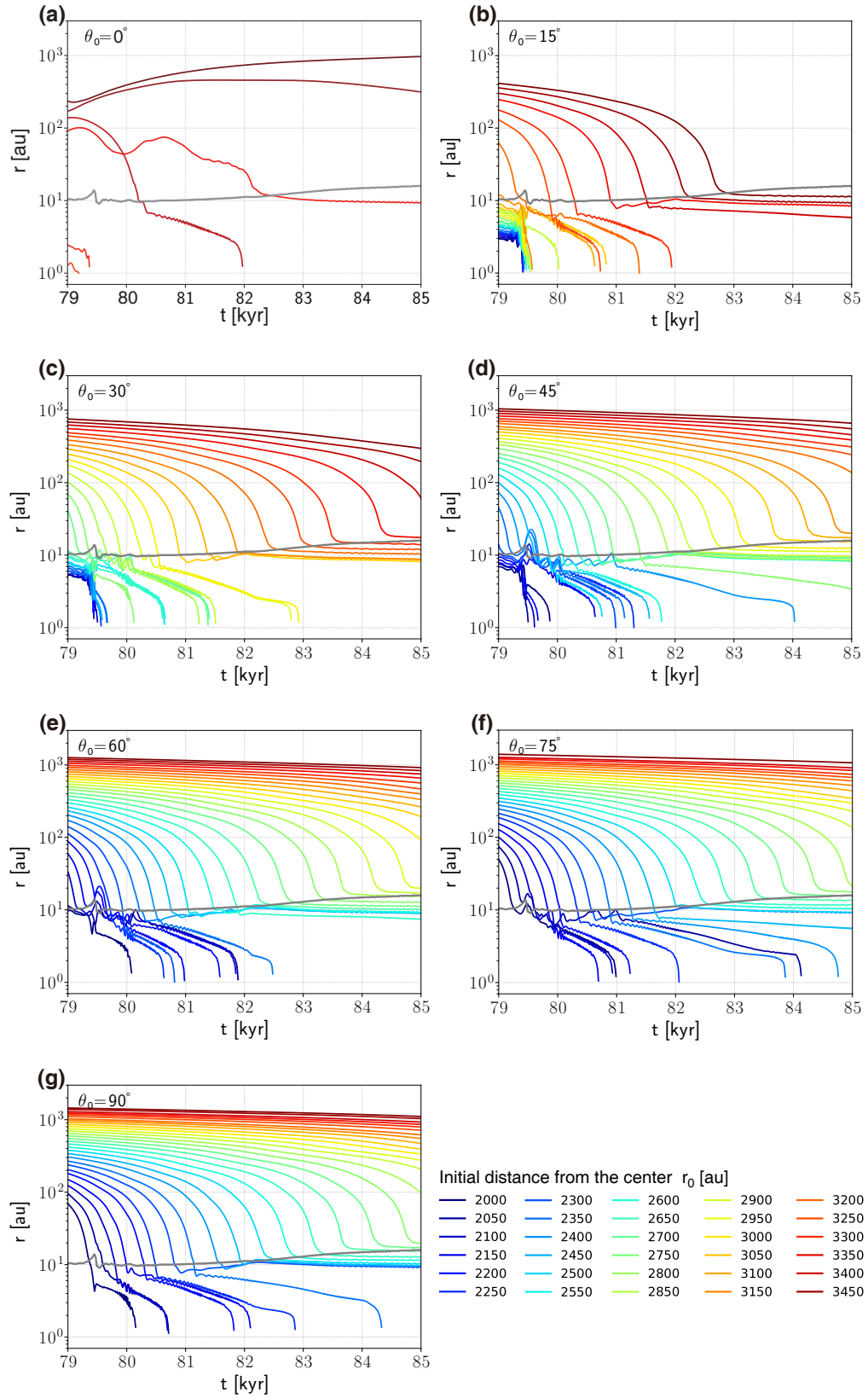


Figure 4. As Fig. 3, for $a_d = 1000 \mu\text{m}$.

for $a_d = 0.01 \mu\text{m}$ (Fig. 3), the dust particles have three major paths, falling onto the sink, being trapping by the rotationally supported disk, and being ejected by the outflow.

Most of the dust particles plotted in Fig. 4 accrete onto the disk. Ejection by the outflow can be seen for only a few particles with $\theta_0 = 0^\circ$ (Fig. 4a). In Fig. 4a, we can confirm that the distance from the center continues to increase with time for one particle ($r_0 = 3450 \text{ au}$), which is outflowing from the center. The particles with $r_0 = 3400, 3350, \text{ and } 3300 \text{ au}$ are entrained by the outflow and their distances initially increase but then decrease, indicating that they fall to the center. For $\theta_0 \neq 0$, the dust particles orbit within the disk after they reach the disk. In Fig. 4b-g, the dust particles initially placed in the range of $r_0 \lesssim 2500 \text{ au}$ finally falls onto the sink. On the other hand, the particles initially placed in the range $r_0 \gtrsim 2500 \text{ au}$ maintain relatively constant distances from the center by the end of the simulation after they enter the disk. The rotationally supported disk has a size of $\sim 10\text{--}20 \text{ au}$ and these particles move with almost the same orbit of $r \sim 10\text{--}20 \text{ au}$, which is the outer disk region or near the outer edge of the disk.

Comparing Fig. 3 and Fig. 4 shows that the fraction of particles falling onto the disk is larger for dust particles with $a_d = 1000 \mu\text{m}$ than for those with $a_d = 0.01 \mu\text{m}$. The dust particles with a size of $1000 \mu\text{m}$ are initially more decoupled from the gas than those with a size of $0.01 \mu\text{m}$, as described in Paper I. Thus, large dust particles tend to fall onto the central region where the disk forms, partially ignoring the gas drag in the infalling envelope. For dust with $a_d = 1000 \mu\text{m}$ (Fig. 4), the dust particles orbiting in the circumstellar disk are initially distributed in the range $\theta_0 = 15\text{--}90^\circ$, where many particles maintain their distances from the center in the range $10\text{--}20 \text{ au}$. Note that one particle ($r_0 = 3300 \text{ au}$) in Fig. 4a survives in the disk without falling onto the sink for $\theta_0 = 0^\circ$. On the other hand, a large fraction of the dust particles with $a_d = 0.01 \mu\text{m}$ (Fig. 3) initially distributed in the range $\theta_0 = 15\text{--}45^\circ$ are ejected by the outflow, after initially moving towards the center. Thus, during the simulation, the number of dust particle orbiting within the circumstellar disk is larger for a size of $a_d = 1000 \mu\text{m}$ than for a size of $a_d = 0.01 \mu\text{m}$.

In the above, we only showed the behavior for dust particles with sizes of $a_d = 0.01$ and $1000 \mu\text{m}$ (i.e., the smallest and largest dust particles considered in this study and Paper I). In the following, we describe the dust motion for other particle sizes ($a_d = 0.1, 1, 10, 100 \mu\text{m}$). The behavior of the particles with $a_d = 0.1, 1, 10 \mu\text{m}$ is the same as for $a_d = 0.01 \mu\text{m}$. Fig. 14 of Paper I showed that the dust abundances of the envelope, protostar, disk, and outflow are the same (or do not change over time) for dust particles in the size range $a_d = 0.01\text{--}$

10 μm . The Stokes numbers for these particles are much less than unity over the simulation, indicating that these particles are well coupled with the gas at all times¹. Therefore, there is no significant difference in the behavior of these particles. On the other hand, the abundance of particles with $a_d = 100 \mu\text{m}$ is different from that of particles with $a_d \leq 10 \mu\text{m}$, but is almost the same as for the case of $a_d = 1000 \mu\text{m}$, because the Stokes number sometimes exceeds unity for these particles (Fig. 17 of Paper I). For this reason, we consider particles with sizes of 0.01 and 1000 μm to illustrate the typical motion of dust grains with different sizes.

3.2.2 Dust motion within the disk

As described in §3.2.1, the dust particles enter the disk when they are not ejected by the outflow. Within the disk, some particles survive without falling onto the disk. Figs. 3 and 4 show that there is a wide range of initial zenith angle $\theta_0 = 15\text{--}90^\circ$ for which the dust particles continue to orbit around 10–20 au. These ‘non-drifting’ dust particles may provide a solution to the radial drift barrier problem, which is one of the most important issues in theoretical planet formation scenarios. In the following, we focus on the trajectories of such particles.

Fig. 5 shows the trajectory of a dust particle with a size of $a_d = 0.01 \mu\text{m}$, initially placed at $(r_0, \theta_0, \phi_0) = (1500 \text{ au}, 90^\circ, 0^\circ)$. Note that this particle moves only on the $z = 0$ plane because it is initially placed on the equatorial plane. After the dust particle reaches the rotationally supported disk, it orbits 30 times around the center, keeping a distance of ~ 10 au from the center. As the figure shows, the particle does not fall to the center by the end of the calculation. Although we only plot the trajectory of a single particle in Fig. 5, all particles having $\theta_0 = 90^\circ$ continue to orbit around the protostar without falling onto the sink after they reach the rotationally supported disk. Interestingly, such particles maintain an orbital radius of $\sim 10\text{--}20$ au during the calculation, as seen in Figs. 3 and 4.

Next, we describe the trajectory of a dust particle that ultimately falls onto the sink. Fig. 6 shows the trajectory of a particle with $a_d = 0.01 \mu\text{m}$, initially placed at $(r_0, \theta_0, \phi_0) = (1900 \text{ au}, 45^\circ, 0^\circ)$. As seen in the right panel of Fig. 6, the particle gradually approaches the equatorial plane while going around the center before it enters the disk region. This particle enters the disk from the vertical direction, whereas the particle shown in Fig. 5, initially

¹ The definition of the Stokes number in Paper I is slightly different from that in the present paper (for details, see §2.3.1 of Paper I and §3.3).

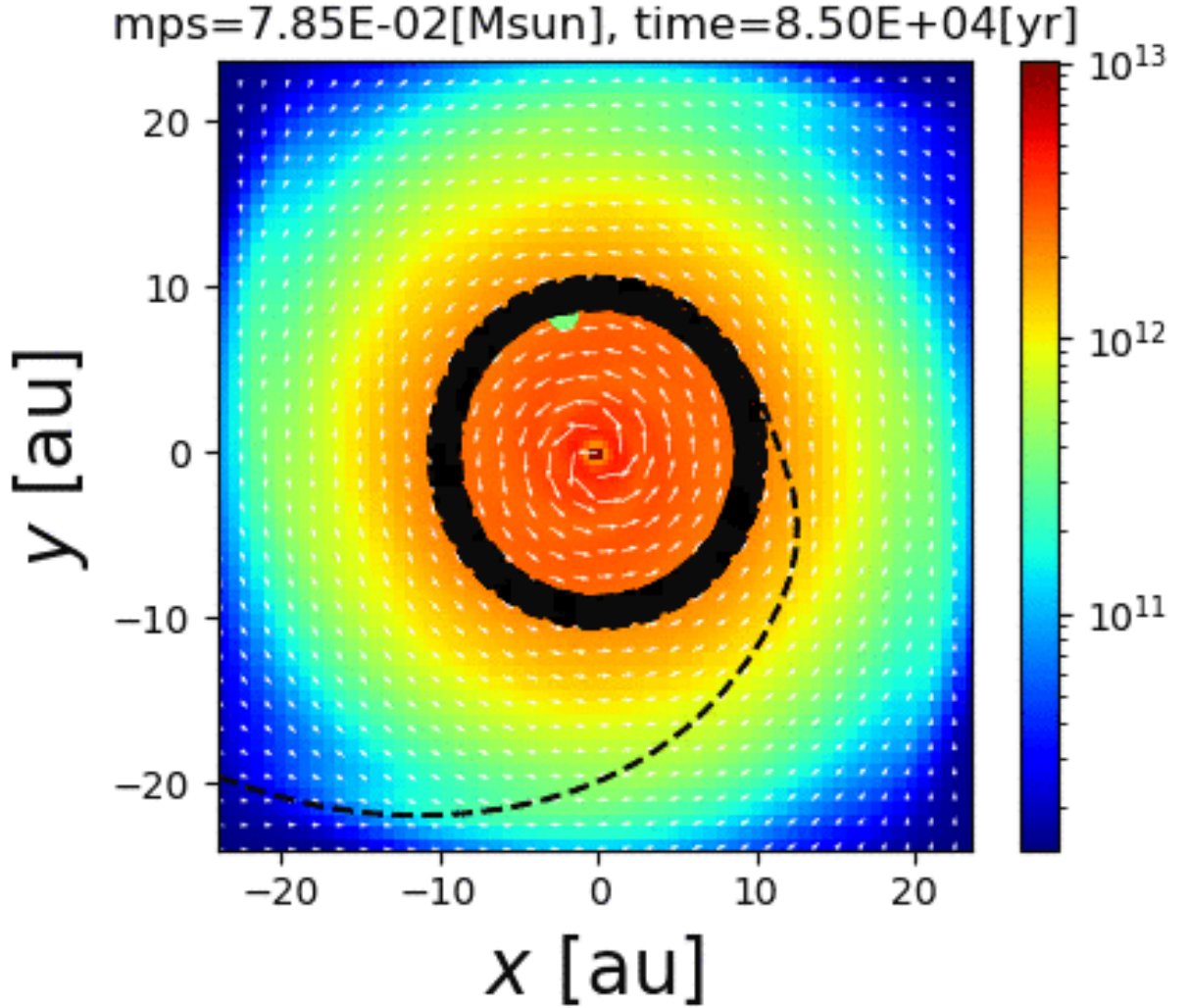


Figure 5. Trajectory of a dust particle (black broken line) superimposed on gas density (color) and velocity (arrows) distributions on the $z = 0$ plane. The particle is initially placed at $(r_0, \theta_0, \phi_0) = (1500 \text{ au}, 90^\circ, 0^\circ)$ and has a size of $a_d = 0.01 \mu\text{m}$. The protostellar mass and elapsed time are given above the plot.

placed on the equatorial plane, enters the disk from the disk outer edge on the equatorial plane. As seen in the left panel of Fig. 6, the particle gradually falls toward the center after it reaches the equatorial plane. The particle orbits around the center for about 4000 yr, slowly moving in a radial direction, while the distance from the center continues to decrease. The particle finally falls onto the sink (or protostar).

Although we only show two typical cases above, the same trend can be seen for other particles. When the dust particles are initially placed near the center (small r_0), they spiral to the sink after reaching the equatorial plane of the disk. The orbital radii for these particles are $r \lesssim 10 \text{ au}$ when they reach the equatorial plane. Dust particles initially placed far from the center (large r_0) settle around $r \gtrsim 10 \text{ au}$ in the disk by the end of the simulation.

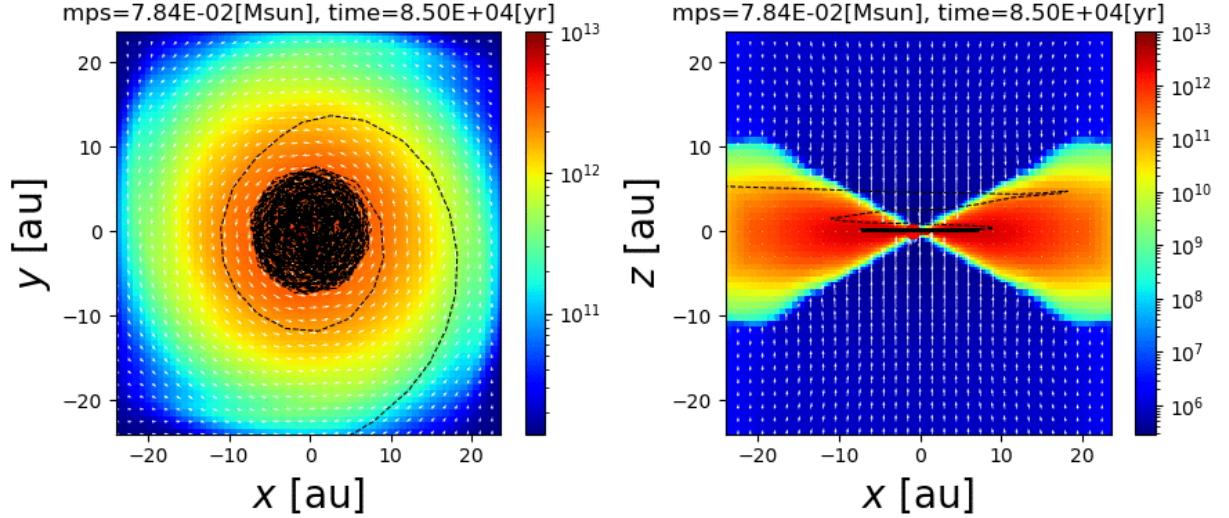


Figure 6. Trajectory of a dust particle (black broken line) superimposed on gas density (color) and velocity (arrows) distributions on the $z = 0$ (left) and $y = 0$ (right) planes. The particle is initially placed at $(r_0, \theta_0, \phi_0) = (1900 \text{ au}, 45^\circ, 0^\circ)$ and has the size of $a_d = 0.01 \mu\text{m}$. The protostellar mass and elapsed time are given above the plot.

Thus, it can be concluded that dust particles will survive without falling onto the sink when they have an orbital radius of $\gtrsim 10 \text{ au}$. These particles tend to reach the outer disk region ($\simeq 10\text{--}20 \text{ au}$), passing through the disk outer edge, as shown in Fig. 5.

3.3 Dust coupling in the disk

In section §3.2, we presented dust trajectories that are not expected based on classical planet formation scenarios. In this subsection, we investigate whether the dust particles that move in the disk are coupled with the gas.

In §3.2, we showed curious behavior of dust grains, in which some dust grains continue to orbit at the same orbital radius without moving toward the center. If the dust grains are strongly coupled with the gas in the disk, the dust motion should coincide with the gas motion. If this is the case, the gas motion can explain why some dust particles maintain an orbit around $r \simeq 10\text{--}20 \text{ au}$. The gas density is higher in the disk than in the envelope and thus, assuming same-sized dust particles, the coupling between the dust particles and gas is stronger in the disk than in the envelope. To quantitatively evaluate how strongly a dust particle is coupled with the gas in the disk, we use the Stokes number St , defined as

$$St = \frac{t_s}{t_K}, \quad (1)$$

where t_K is the Keplerian timescale Ω_{kep}^{-1} ($= (GM_{\text{ps}}/r)^{-1/2}$).

Figs. 7 and 8 show the time evolution of the Stokes number for dust particles orbiting

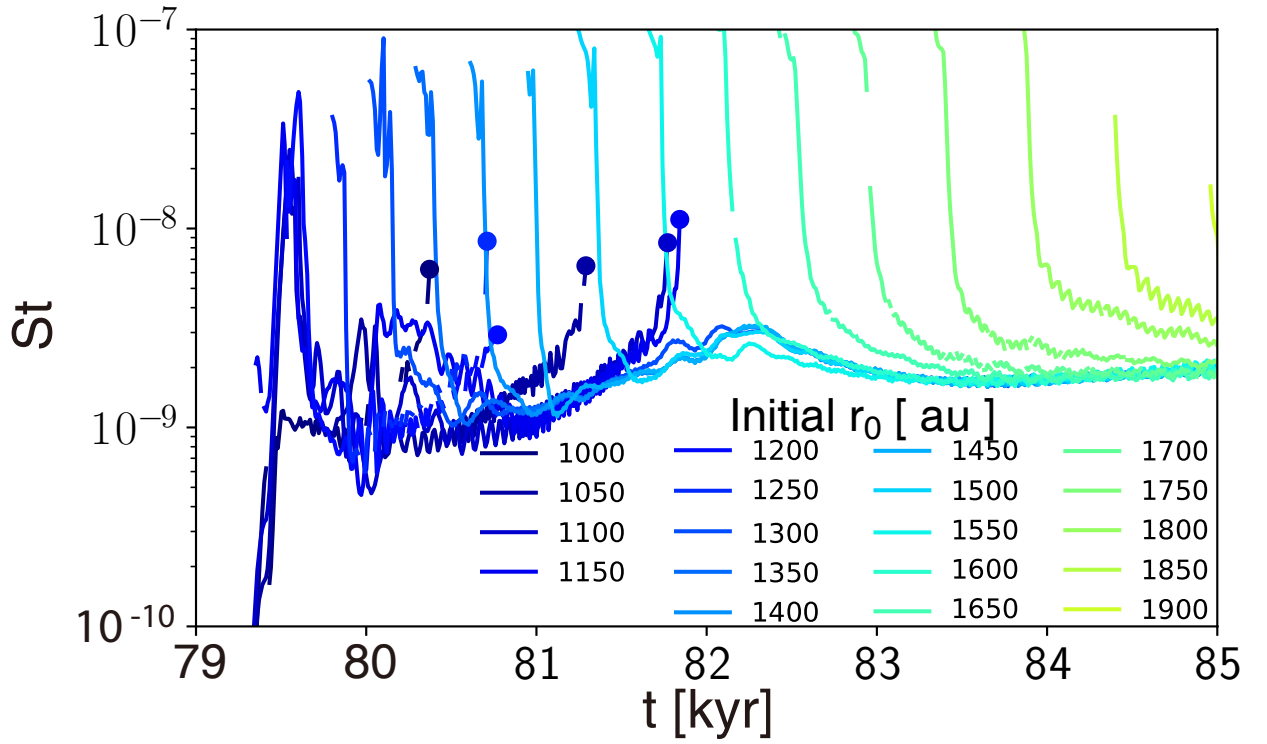


Figure 7. Time evolution of the Stokes number for dust particles with $a_d = 0.01 \mu\text{m}$. St is defined in equation (1). Lines are plotted only when the particles are moving in the disk region. The color indicates the initial radius r_0 and is the same as that in Fig. 3. Filled circles represent particles that fall onto the sink.

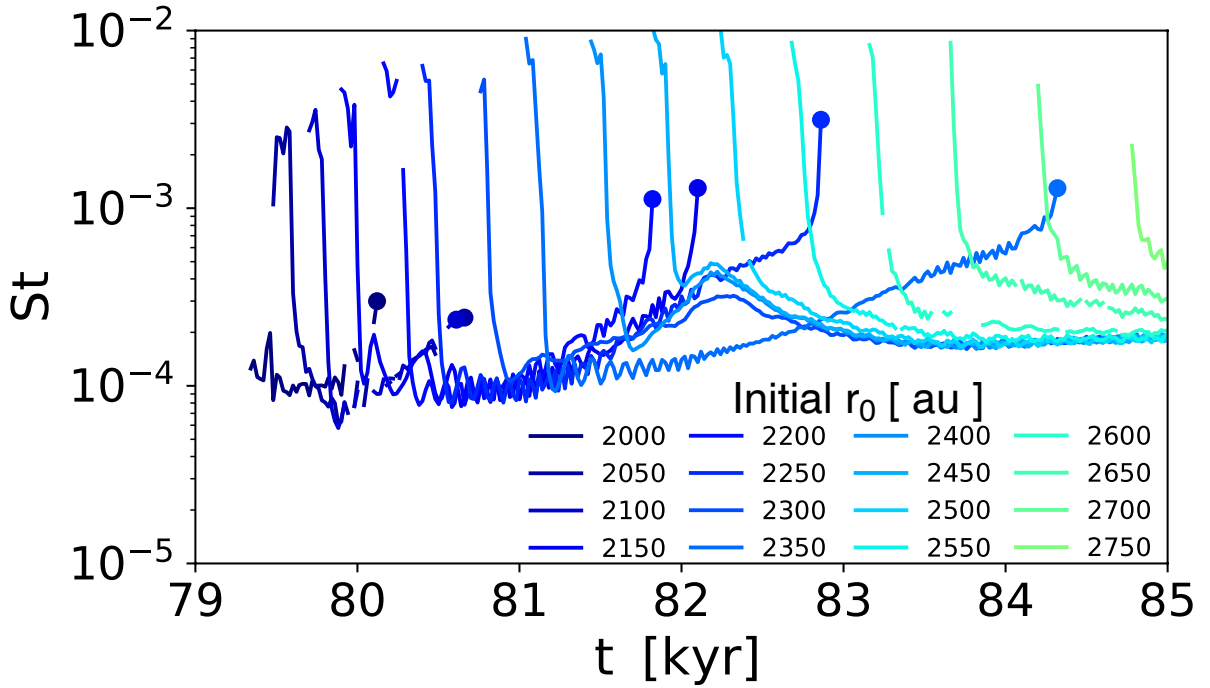


Figure 8. As Fig. 7, for particles with $a_d = 1000 \mu\text{m}$. The color indicates the initial radius r_0 and is the same as that in Fig. 4.

within the disk with $a_d = 0.01$ and $1000 \mu\text{m}$. According to Paper I, the disk is defined as the region where the rotational velocity dominates the infall velocity ($v_\phi > 2|v_r|$) and the gas is rotationally supported ($v_\phi > 0.6 v_K$, where v_K is the Keplerian velocity). In the figures, a broken part of the line indicates that the dust particle is temporarily located outside the disk. When the line is broken while St decreases, the particle has temporarily moved into the envelope near the disk. A filled circle indicates the epoch at which the dust particle falls onto the sink before the end of the calculation ($t < 85 \text{ kyr}$). A sudden increase in St is caused by a sudden decrease in the radius of a particle in the disk.

Fig. 7 shows that dust particles entering the disk from the envelope have $\text{St} \ll 1$. In particular, the Stokes number for dust particles orbiting at $r \simeq 10\text{--}20 \text{ au}$ is $\text{St} \sim 10^{-9}$, indicating that they are strongly coupled with the gas. Fig. 8 plots the time evolution of St for dust with $a_d = 1000 \mu\text{m}$, which is the maximum dust size prepared in this study. When the gas has the same physical quantities, larger dust particles tend to be more easily decoupled from the gas due to their longer stopping time. However, even for dust particles having $a_d = 1000 \mu\text{m}$, the Stokes number is $\text{St} \sim 10^{-4}$. Thus, such large particles are also coupled with the gas in the disk.

The St for particles with $a_d = 1000 \mu\text{m}$ is about five orders of magnitude larger than that for dust particles with $a_d = 0.01 \mu\text{m}$. This is because the Stokes number is proportional to the dust size as $\text{St} \propto a_d$. Therefore, we can conclude that the result that some dust particles orbit at the same orbital radius instead of gradually falling toward the central star can be attributed to the gas motion, that is, the gas motion on the equatorial plane in the disk prevents the dust particles from accreting onto the central protostar. Thus, the dust grains are controlled by gas motion in the disk independent of the dust size in the early star formation stage.

4 DISCUSSION

4.1 Angular momentum transport and gravitational instability

As shown in §3.3, a portion of the dust particles keep orbiting around $r \simeq 10\text{--}20 \text{ au}$ in the disk without falling onto the sink. The dust particles eternally orbiting in the disk are strongly coupled with the gas, because the gas density is sufficiently high and the Stokes number is much smaller than unity. Thus, to understand why some of the dust is captured in

an orbit, it is important to investigate the physical properties of the gas. In this subsection, we investigate the characteristics of the gas disk around the central region.

First, we focus on the angular momentum transport in the disk. To extract the structure in the high-density region, we plot the density distribution in the density range $n > 2.5 \times 10^{12} \text{ cm}^{-3}$ in Fig. 9. The figure clearly shows that the local high-density region has a spiral structure which extends to ~ 10 au. The elapsed time and spatial scales are the same as in the bottom left panel of Fig. 1. Previous studies have shown the formation of a spiral structure driven by gravitational instability (Tomida et al. 2017). Since the high-density spiral arm has a non-axisymmetric structure, the angular momentum could be transported by the gravitational torque.

To validate the gravitational instability in the disk, the Toomre Q parameter is plotted in Fig. 10. The definition and calculation method of the Q parameter in the disk are described in Paper I and Tomida et al. (2017). The figure indicates that $Q < 2$ in the range $7 \text{ au} \lesssim r \lesssim 20 \text{ au}$. Thus, a spiral structure will naturally develop in this region. The spiral arms extend to ~ 10 au (Fig. 9), while the Q parameter has a local minimum around $r \sim 10$ – 15 au (Fig. 10). The position of the spiral arms is not in complete agreement with the region having a local minimum of Q , as previously shown in Tomida et al. (2017). The angular momentum should be transported outward due to gravitational torque caused by the spiral arms inside the $\lesssim 10$ au region of the disk. In contrast, the gas distributed in the outer disk region of $r \gtrsim 10$ au should gain angular momentum due to angular momentum conservation. Thus, a parcel of gas can stay around $r \simeq 10$ – 20 au without moving inward. Therefore, the gas around $r \gtrsim 10$ au orbits at almost the same radius while maintaining its angular momentum. As seen in Figs. 3–8, the dust particles in the disk are strongly coupled with the gas. As a result, the dust particles located around $r \gtrsim 10$ au receive angular momentum from the gas and survive to orbit in the disk without causing inward radial drift.

To understand the behavior of dust particles, the time evolution of the specific angular momentum for the two dust particles shown in Figs. 5 and 6 is plotted in Fig. 11. In the figure, a sudden drop at $t \sim 81$ kyr indicates that the particles enter the disk from the infalling envelope. The dust particle plotted by the blue line gradually loses its specific angular momentum in the disk and finally falls onto the sink. The dust particle plotted by the red line increases its specific angular momentum during $t = 81.2$ – 82.5 kyr, and then it has an almost constant specific angular momentum by the end of the simulation. Although the specific angular momenta of the two particles are almost the same before they enter the

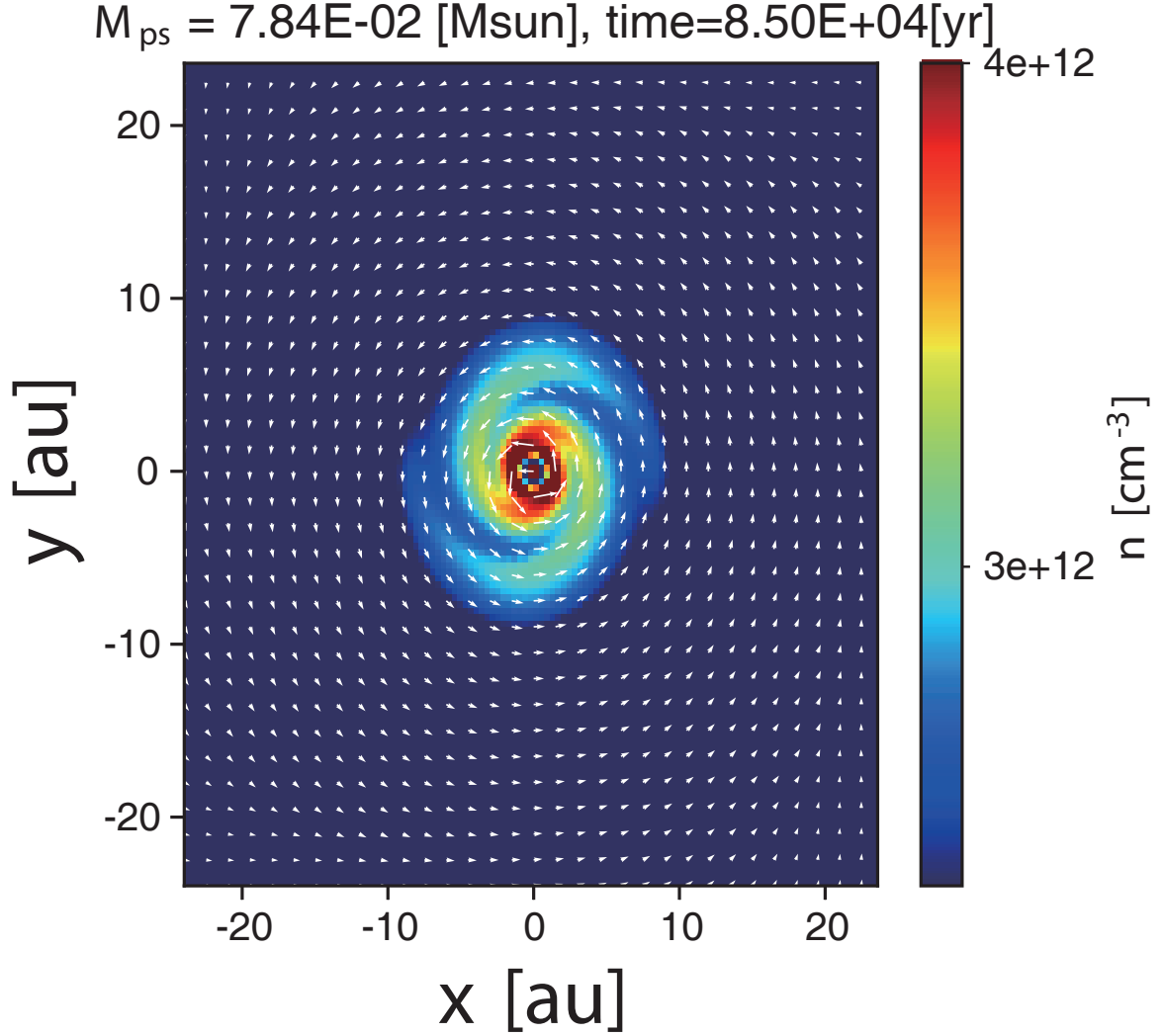


Figure 9. Same as the bottom left panel of Fig. 1, with a different color (or density) range.

disk, their trajectories are different (see Figs. 5 and 6). The particle shown in Fig. 5 enters the disk from the side on the equatorial plane, while the particle shown in Fig. 6 enters the disk from above. The different trajectory histories in the envelope result in different outcomes.

In addition to the gravitational torque, the angular momentum can be transported by magnetic effects. Plasma β is a useful index to evaluate whether magnetic effects play a role in angular momentum transfer. Fig. 12 plots plasma $\beta = P_{\text{gas}}/P_{\text{mag}}$ on the equatorial plane, where P_{gas} and P_{mag} are the gas and magnetic pressure, respectively. The figure shows that the plasma beta around $r \sim 10$ au is as large as $\beta \sim 10^5$, indicating that magnetic effects can be negligible for transporting the angular momentum in the rotationally supported disk.

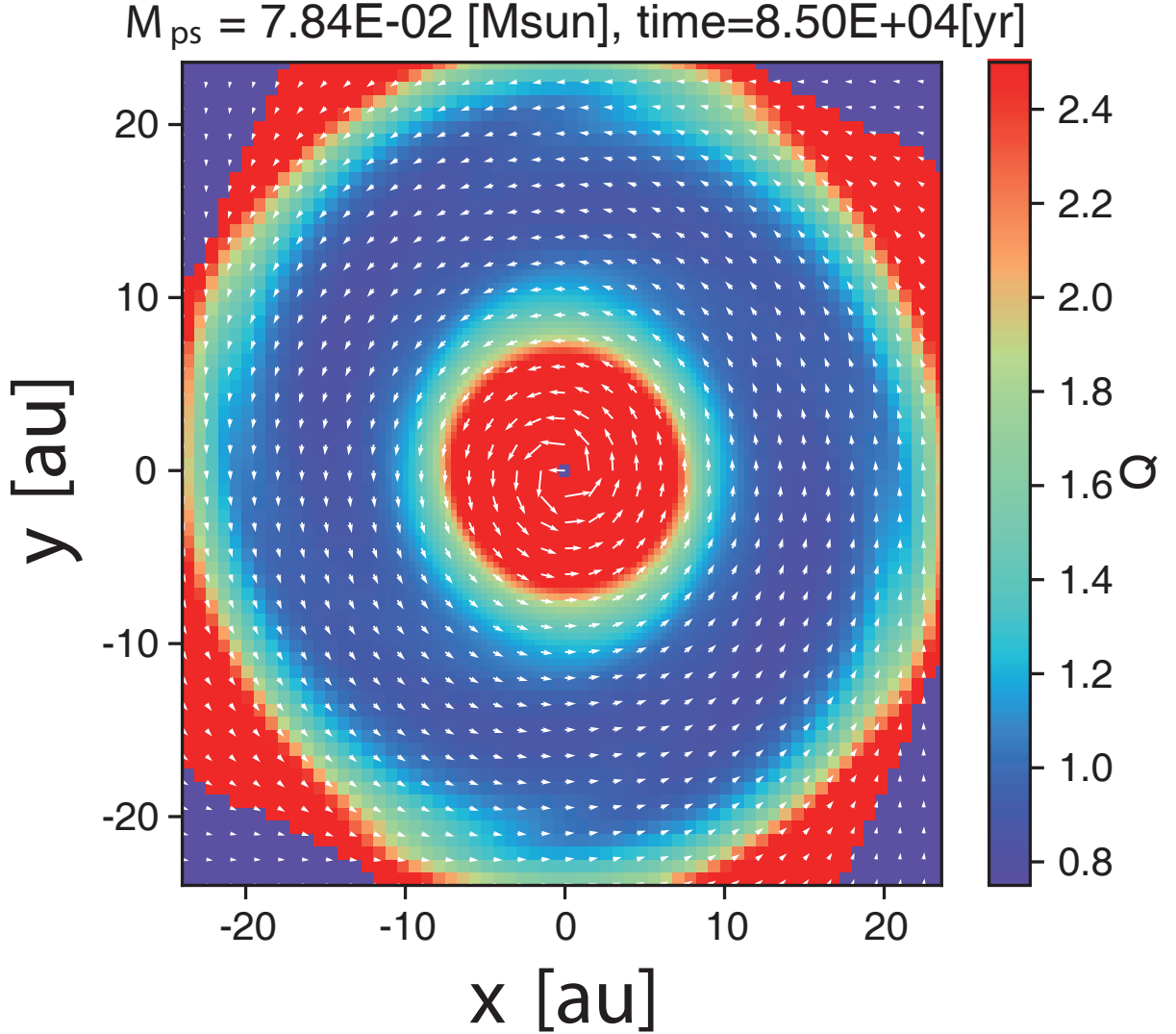


Figure 10. Toomre’s Q parameter (color) for the disk plotted on the $z = 0$ plane, in which the physical quantities are integrated in the vertical direction within the disk and are averaged.

4.2 Difference from classical planet formation scenario

The MMSN is often used as a disk model in the classical planet formation scenario. The gas disk considered in this study is different from the MMSN. In this study, we simulated the formation and evolution of a disk from a prestellar cloud core (or a molecular cloud core). Molecular cloud cores are characterized by many observations (e.g., [Tokuda et al. 2020](#)). We self-consistently include both the (disk) self-gravity and magnetic fields in our cloud core collapse simulation. Our simulation shows a different dust behavior, which has not been reported in previous studies. The crucial difference between our study and previous studies is the radial inward movement of the dust. In previous studies, the dust gradually moves inward, which is called the radial drift problem (e.g., [Weidenschilling 1977](#)). We show that

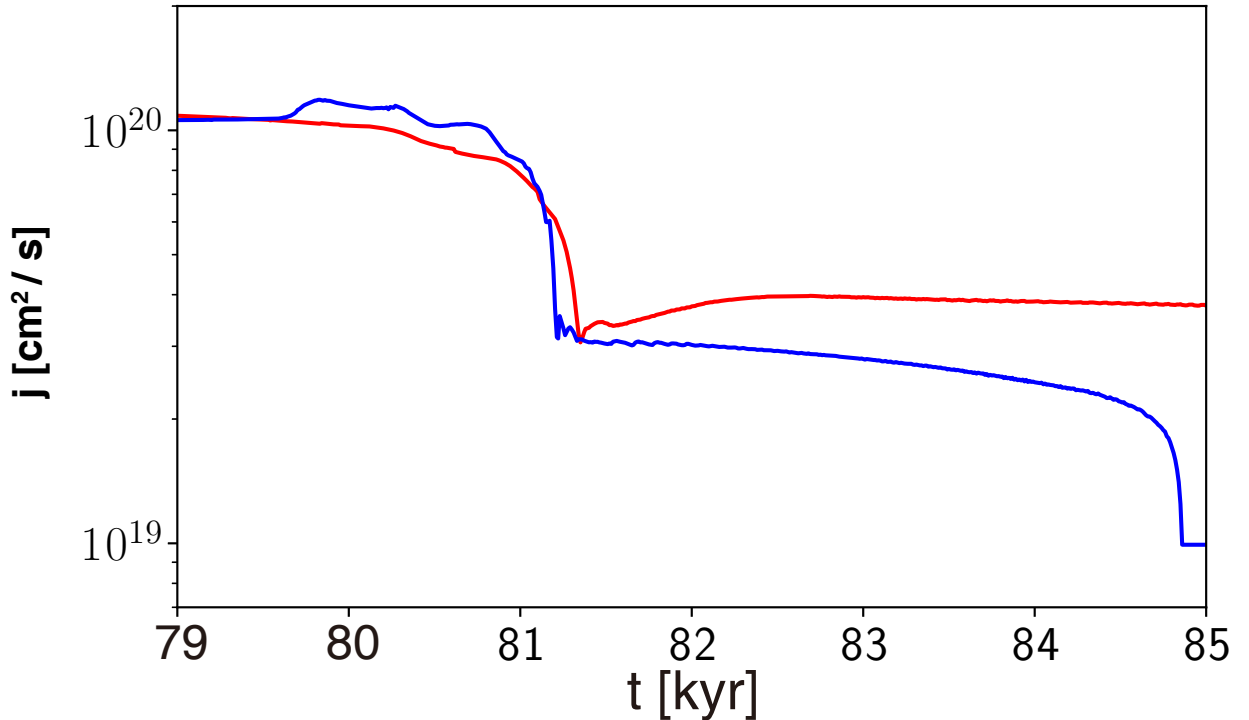


Figure 11. Time evolution of specific angular momentum for two selected dust particles. The red line corresponds to a dust particle orbiting around 10 au without showing significant inward radial movement, shown in Fig. 5. The blue line corresponds to the dust particle shown in Fig. 6, in which the particle falls onto the sink while orbiting in the disk.

a portion of the dust particles does not monotonically fall onto the central protostar, but that some particles can survive and orbit in the outer disk region. Many theoretical studies have proposed possible solutions to avoid the radial drift problem. In terms of a dust model, [Okuzumi et al. \(2012\)](#) considered the internal structure of dust and showed that porous aggregates can solve the radial drift problem. In addition, the radial drift problem can be overcome by preparing artificially adjusted gas disks. For example, [Takahashi & Muto \(2018\)](#) suggested a gas disk model assuming an MHD disk wind producing a pressure bump within the disk. In such a disk model, dust grains concentrate around the pressure bump and dust growth is significantly promoted before the dust falling onto the central protostar.

As described above, our simulation shows that a non-axisymmetric structure induced by gravitational instability develops in the disk and can prevent the radial drift of dust. Our disk structure is obtained from a three-dimensional MHD simulation starting from the molecular cloud core and is suitable for investigating the initial conditions of planet formation. However, we ignore the dust growth and porosity. The dust growth is discussed in the next section, while the porosity will be focused in future studies.

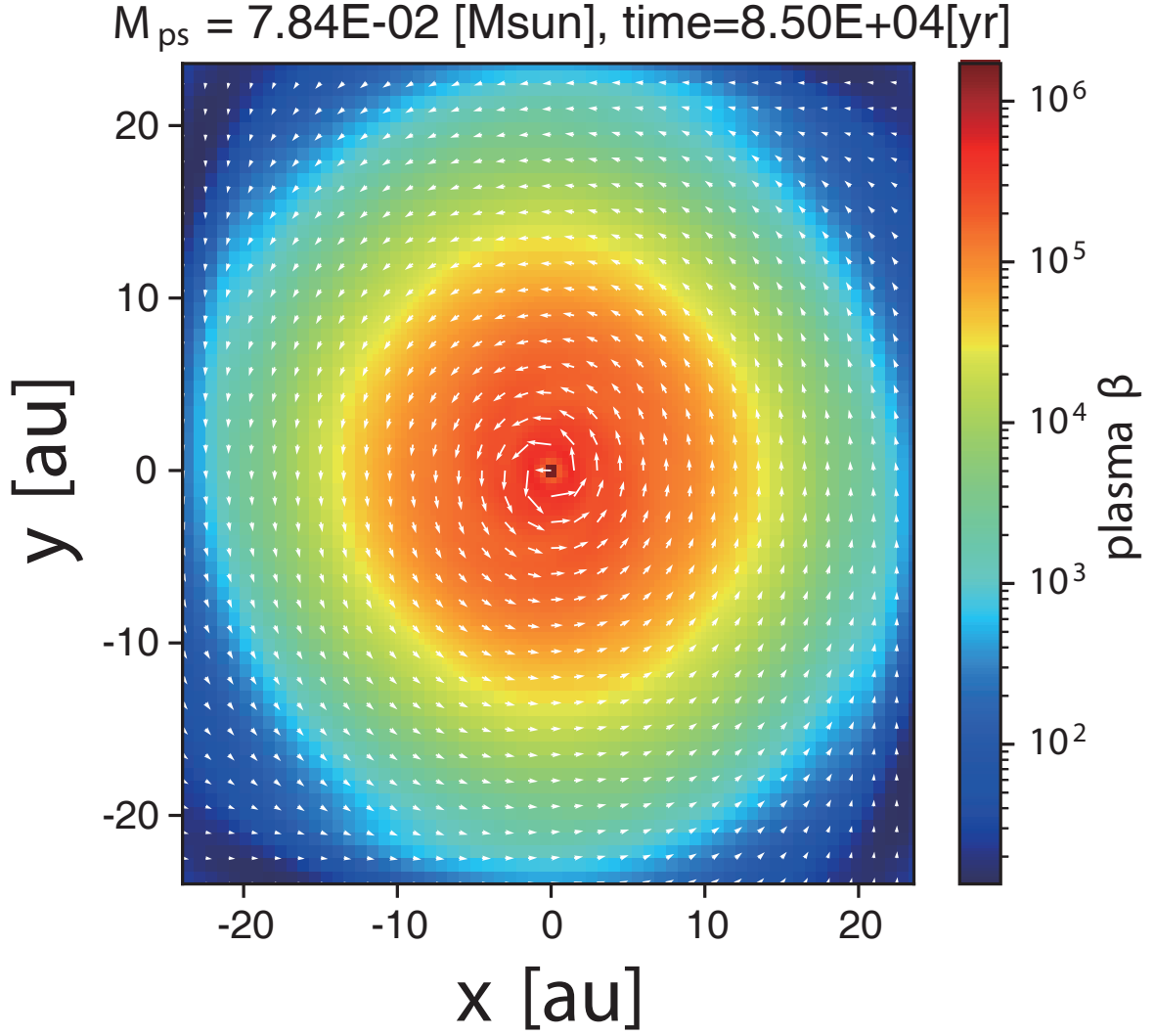


Figure 12. As Fig. 10, with the color indicating the plasma β .

4.3 Dust Growth

The growth of dust particles is ignored in our method, as described in §4.2 and Paper I. Instead, we adopt different-size set of dust particles in the range $0.01 \mu\text{m} \leq a_d \leq 1000 \mu\text{m}$. The simulation shows that the dust particles of any size remain in the outer disk region for > 3000 yr, as described in §3.2. Thus, the growth of dust particles can be expected in such a region (Fig. 5). This subsection discusses the possibility of the growth of dust particles orbiting around the outer disk region.

The evolution of dust peak (or typical) mass m_d in the Lagrange form can be described (Ormel 2014; Sato et al. 2016; Okuzumi et al. 2016; Arakawa et al. 2021) as

$$\frac{dm_d}{dt} = \frac{2\sqrt{\pi}a_d^2 \Delta v_d \Sigma_d}{h_d}, \quad (2)$$

where Σ_d and h_d are the surface density and scale height of the dust, and Δv_d is the relative velocity between dust particles. We consider the collisional growth of dust grains composed of single-sized particles with equation (2). As described in §3.3, the dust particles of any size adopted in this study are well coupled with the gas within a rotationally supported (or Keplerian) disk. Thus, the dust scale height h_d is assumed to be equal to the gas scale height h_g . In addition, the disk surface density can be described as $\Sigma_d = f_{dg}\Sigma_g$, where $f_{dg}(= 0.01)$ is the dust-to-gas mass ratio. Note that the f_{dg} is considered not to be (significantly) changed during the simulation, as shown in Paper I. Then, with the gas mass density ρ_g , we replace (Σ_d/h_d) into $(f\Sigma_d/h_d) = f\rho_g$ in equation (2). Thus, equation (2) can be written as

$$\frac{dm_d}{dt} = 2\sqrt{\pi}a_d^2\Delta v_d f\rho_g. \quad (3)$$

In addition, since we assume the spherical dust particles, the mass of each dust particle is described as

$$m_d = \frac{4\pi a_d^3 \rho_s}{3}, \quad (4)$$

where $\rho_s(= 1 \text{ g cm}^{-3})$ is the material density of dust grains, in which the dust grains are assumed to be composed of ice (Paper I). With equations (2)–(4), we can estimate the growth timescale of dust grains t_{grow} with the dust mass m_d and dust size a_d (Arakawa et al. 2021; Tsukamoto et al. 2021b) as

$$\begin{aligned} t_{\text{grow}} &\equiv \left(\frac{1}{a_d} \frac{da_d}{dt}\right)^{-1} = 3 \left(\frac{1}{m_d} \frac{dm_d}{dt}\right)^{-1} \\ &= \frac{2\sqrt{\pi}a_d\rho_s}{\Delta v_d f\rho_g}. \end{aligned} \quad (5)$$

We need the relative velocity between dust particles Δv_d to estimate the growth timescale in equation (5). The relative velocity cannot be estimated in the simulation because the spatial scale between dust particles ($\lesssim 1 \text{ cm}$) and circumstellar disk ($> 10^{14} \text{ cm}$) considerably differs. Thus, we use a simple formulation of the relative velocity used in past studies (Ormel & Cuzzi 2007; Okuzumi et al. 2016; Arakawa et al. 2021; Shibaïke & Mori 2022) as

$$\Delta v_d = \sqrt{3\alpha \text{St}} c_s, \quad (6)$$

where α , St and c_s are the parameter characterizing turbulence or viscosity on a scale comparable to the size of dust particles, the Stokes number, and the sound speed of the outer disk region, respectively. Substituting equation (6) into equation (5), the growth timescale can be written as

$$t_{\text{grow}} = \frac{2\sqrt{\pi}a_d\rho_s}{f\rho_g} (3\alpha \text{St})^{-1/2} c_s^{-1}. \quad (7)$$

In the following, we estimate the dust growth timescale (eq. [7]) using our simulation results.

As shown in Figures 3–5, the dust particles of any size remain (or continue to orbit) around ~ 10 au far from the central protostar. In such a region, the gas density is as high as $\rho_g \sim 10^{-11} \text{ g cm}^{-3}$ and the temperature is $T \simeq 100 \text{ K}$ (see Fig. 5 and Paper I). Note that the $\rho_g \sim 10^{-11} \text{ g cm}^{-3}$ roughly corresponds to the lowest density of the magnetically inactive region where the magnetic field dissipates (Nakano et al. 2002; Machida et al. 2007). A rotationally supported disk forms in such a region in the early star formation stage (Machida & Matsumoto 2011). Next, using simulation results (Paper I and Figs. 7 and 8), we relate the dust size a_d to the Stokes number St in the outer disk region (~ 10 au) as

$$St \simeq 10^{-7} \left(\frac{a_d}{10^{-6} \text{ m}} \right). \quad (8)$$

Using these simulation results, we can rewrite the growth timescale given by equation (7) as

$$t_{\text{grow}} = 29.2 \left(\frac{a}{10^{-4} \text{ cm}} \right)^{1/2} \left(\frac{\rho_s}{1 \text{ g cm}^{-3}} \right) \left(\frac{f}{0.01} \right)^{-1} \left(\frac{\rho_g}{10^{-11} \text{ g cm}^{-3}} \right)^{-1} \left(\frac{\alpha}{0.01} \right)^{-1/2} \left(\frac{T}{100} \right)^{-1/2} \text{ yr}, \quad (9)$$

where the sound speed $c_s = 7.0 \times 10^4 (T/100)^{1/2}$ is used. For simplicity, we describe the growth timescale as a function of only the dust size a_d as

$$t_{\text{grow}} = 29.2 \left(\frac{a}{10^{-6} \text{ m}} \right)^{1/2} \text{ yr}. \quad (10)$$

Equation (10) indicates that the dust grains with a size of $1 \mu\text{m}$ grow in ~ 30 yr in the outer disk region.

As described in §3, the dust particles entered from the horizontal direction (or the disk outer edge on the equatorial plane) orbit around ~ 10 au within the disk without falling onto the central protostar. The Keplerian timescale is given by

$$t_{\text{Kep}} = 100 \left(\frac{M_*}{0.1 M_\odot} \right)^{-1/2} \left(\frac{r}{10 \text{ au}} \right)^{3/2} \text{ yr}. \quad (11)$$

The dust (and gas) particles in the outer disk region survive for > 3 kyr corresponding to > 30 orbital periods at $r = 10$ au (see §3.3). Adopting the growth timescale being equal to $30 t_{\text{Kep}} = 3$ kyr, we can estimate the maximum dust size possible to be grown in the outer disk region with $t_{\text{grow}} = 30 t_{\text{Kep}}$. With equation (10), we can estimate the maximum dust size as $a_d = 1.06 \text{ cm}$ when the dust particle orbit around ~ 10 au for ~ 3 kyr. In our calculation, the dust particle of any size (0.01 – $1000 \mu\text{m}$) are well coupled with the gas in the disk (§3.3). Thus, the growth of the dust particles should be justified until the dust size reaches $a_d \simeq 0.1 - 1 \text{ cm}$.

Recently, [Tsukamoto et al. \(2021b\)](#), [Tu et al. \(2022\)](#) and [Bate \(2022\)](#) investigated the dust growth in the early star formation stage with (magneto)hydrodynamic simulations. The dust grows to reach $a_d \sim 0.1 - 1$ cm in [Tsukamoto et al. \(2021b\)](#) and [Tu et al. \(2022\)](#), which is consistent with our estimate above. On the other hand, [Bate \(2022\)](#) showed that dust grains only grow to about 0.01 cm. However, since he investigated only the very early stage of star formation, his result does not contradict our estimate.

We stopped the calculation before the disk sufficiently grows due to the limitation of computational resources. Thus, the dust particles may grow larger than 1 cm in size in a further evolutionary stage. Equation (8) indicates that the $St \leq 0.1$ sustains as long as the dust size is smaller than $a_d \lesssim 1$ m. Equation (10) indicates that the dust can grow to reach $a_d = 1$ m for about 3×10^4 yr. When the dust grains have a size of $a_d = 1$ m, the relative velocity is $\Delta v_d = 38 \text{ m s}^{-1}$ (eq. 6) and is still comparable to or smaller than the fragmentation velocity for the dust composed of ice grains $v_{\text{frag}} = 20 - 70 \text{ m s}^{-1}$ (e.g. [Wada et al. 2013](#); [Kawasaki et al. 2022](#)). Thus, the dust may grow in the outer disk region until the dust size reaches ~ 1 m. Although we should miss many effects to suppress or promote the dust growth ([Bae et al. 2022](#)), our result implies that the dust can sufficiently grow in the outer disk region. The rapid dust growth is attributed to the high-density and long dynamical timescale (with a small protostellar mass and large radius), which is realized in the early stage of star formation.

4.4 Observations of large-sized dust grains within protostellar outflow and envelope

The dust growth in the disk would be verified in the observations of protostellar outflows. [Kwon et al. \(2019\)](#), [Galamez et al. \(2019\)](#) and [Valdivia et al. \(2019\)](#) have implied the existence of large-sized dust grains ($\gtrsim 10 - 100 \mu\text{m}$) within the envelope. The dust growth timescale within the outflow is as long as $> 10^8$ yr, in which the maximum outflow density $\rho = 10^{-17} \text{ g cm}^{-3}$ (Fig. 2) and $a_d = 100 \mu\text{m}$ are introduced in equation (9). In addition, the dust growth timescale in the envelope is $> 10^6$ yr with the density of $\rho = 10^{-15} \text{ g cm}^{-3}$. Thus, it is difficult for dust particles to grow to $\sim 100 \mu\text{m}$ in the envelope and outflow.

On the other hand, we have already shown that the protostellar outflow contains $100 \mu\text{m}$ dust grains in our previous study (see Figs. 8 and 12 of Paper I), indicating that the dust grains with a size of $10 - 100 \mu\text{m}$ are (partially) coupled with the gas within the outflow

(see Fig. 13 of Paper I). Although we did not consider the dust growth in this and previous studies, we discuss the growth timescale of dust grains in §4.3. The dust grains can grow up to at least ~ 1 cm in size when the grains continue to orbit around the outer disk region (§4.3). Therefore, it is natural that dust grains with a size of $\gtrsim 10 - 100 \mu\text{m}$ are ejected from the circumstellar disk by the outflow. Tsukamoto et al. (2021b) showed that a portion of the dust particles are decoupled from the gas in the outflow and falls into the envelope and disk. As a result, the falling particles can contribute to the increase of the abundance of large-sized dust grains in the envelope. Thus, observing the large-sized grains in the envelope or outflow may be proof of dust growth in the circumstellar disk in the early stage of star formation. We cannot directly show the circulation and growth process of dust grains shown in Tsukamoto et al. (2021b), because the dust growth is not considered in this study. We will investigate it in our future studies.

4.5 Caveats and future perspectives

In addition to Ohmic dissipation, there are two other non-ideal MHD effects, ambipolar diffusion and the Hall effect, which are not considered in our simulation. Although these effects are also important during the star formation process, they are not expected to significantly change the dust trajectories in high-density gas disks, as both ambipolar diffusion and the Hall effect influence the gas dynamics in relatively low-density gas regions (e.g. Koga et al. 2019; Kawasaki et al. 2021). Our simulation settings are the same as in Tomida et al. (2017), which reported that the simulation reproduces the observed disk structure fairly well. We show that dust particles located in the outer disk region do not fall onto the protostar because such particles receive angular momentum from the inner disk region, transported by the gravitational torque. The formation of a gravitationally unstable disk has also been confirmed with non-ideal MHD simulations that include three non-ideal MHD effects, Ohmic dissipation, ambipolar diffusion, and the Hall effect (e.g. Wurster et al. 2019). These simulations also show that angular momentum is transported outward by gravitational instability (or gravitational torque). Thus, suppression of the dust inward motion can be expected as long as the disk is in a gravitationally unstable state or in the main accretion phase.

The magnetic diffusion coefficients of non-ideal MHD effects depend on the dust properties such as size and size distribution of dust grains (Kawasaki et al. 2022). The non-ideal MHD effects or dust properties can influence the properties of protostellar outflows (e.g. Marchand

et al. 2020). The outflow can transport angular momentum from the circumstellar disk. Thus, the change in the efficiency of angular momentum transport due to the outflow should change the disk properties, such as the size and density of the circumstellar disk in the early stage of star formation. As a result, the properties of the region where dust particles continue to orbit should be changed. However, the dust motion in the outer disk region should not be qualitatively changed as long as the gravitationally unstable disk sustains, as described above. On the other hand, the dust growth timescale discussed in §4.3 may be changed according to the properties of both outflow and circumstellar disk.

Finally, we discuss the effect of radiative feedback from the protostar. In this study, we do not consider the issue of radiative transfer. However, radiative heating from the central protostar may influence the disk dynamics. The protostellar accretion luminosity can heat the disk even when the protostellar mass is as small as $\sim 0.1 M_{\odot}$ (e.g. Machida & Hosokawa 2013; Hennebelle et al. 2020). Thus, radiative heating tends to suppress the disk gravitational instability. In addition, viscous heating by differential rotation in the disk and shock heating during accretion from the infalling envelope may affect the disk dynamics. Heating and cooling should be carefully addressed in future studies to more adequately investigate the disk dynamics and behavior of dust grains.

5 CONCLUSION

We investigated the behavior of dust grains in a star-forming cloud. We developed a new method to calculate the behavior of dust grains as Lagrange particles and solve the fluid dynamics in the Eulerian framework to investigate the motion of dust grains in the early star and disk formation stage. We described the implementation and range of application for Lagrange dust particles in Paper I. We also showed the time evolution of dust abundance in the protostar, disk, outflow, and envelope regions in Paper I. The current paper focused on the dust motion and the coupling between dust and gas in the main accretion phase, during which the circumstellar disk gradually grows.

We prepared six different-size set of dust particles in the range $0.01\text{--}1000 \mu\text{m}$ and placed them in a prestellar cloud core. We calculated the evolution of the cloud core until the protostellar mass reaches $0.0784M_{\odot}$, ignoring dust growth. In the gravitationally collapsing cloud, a circumstellar disk forms and drives a protostellar outflow. Although the disk grad-

usually grows in the main accretion phase, the size of the disk is as small as ~ 20 au at the end of the simulation.

A large portion of the large dust particles ($a_d \gtrsim 100 \mu\text{m}$) falls onto the disk, while the outflow can eject a small number. For the small dust particles ($a_d \lesssim 10\text{--}100 \mu\text{m}$), the dust particles initially placed with a small zenith angle $\theta_0 \lesssim 45^\circ$ are ejected by the outflow, where θ_0 is the angle relative to the rotation axis (or the z -axis). Since we already showed the spatial variation in the abundance of different-sized dust grains in Paper I, we did not comment on this in this study.

The motion of dust grains exhibits two trends after they enter the circumstellar disk, dependent on their history or trajectory until they reach the disk, regardless of the dust size. The dust grains slowly move inward and fall onto the sink (or protostar) when they enter the circumstellar disk from above, for which the incidence angle of the dust grains relative to the disk normal is small. In contrast, the dust grains continue to orbit near the outer edge of the disk, neither moving inward nor falling onto the protostar, when they enter the disk from the side or near the equatorial plane with a large incidence angle relative to the disk normal. In other words, dust grains reaching the inner disk region from the upper envelope rapidly fall onto the protostar, while those reaching the outer disk region survive without falling onto the protostar.

We estimated the coupling between dust grains and gas in the disk using the Stokes number to investigate the motion of the surviving dust grains. The Stokes numbers for all dust grains with sizes of $a_d = 0.01\text{--}1000 \mu\text{m}$ are well below unity, indicating that the dust grains are well coupled with the gas in the disk. Thus, the curious behavior of dust grains in the disk could be attributed to the gas motion within the disk.

In the disk, the magnetic field is weak and the plasma beta is very high because of effective magnetic dissipation. Thus, the magnetic field cannot play a role in transporting the angular momentum in the disk. As a result, the disk mass gradually increases without an effective mechanism for angular momentum transfer. This will cause gravitational instability because the mass supply from the infalling envelope to the disk persists in the main accretion phase. We found that a tiny spiral structure develops due to gravitational instability near the disk center. The spiral structure extends to ~ 10 au, while the disk has a radius of ~ 20 au. Thus, the gas and dust particles located at $r \lesssim 10$ au lose their angular momentum due to gravitational torque related to the spiral structure, and they can fall onto the central region.

The gas and dust particles located at $r \gtrsim 10$ au receive angular momentum from the inner gas and dust particles, and survive without falling onto the protostar.

In our simulation, dust particles orbiting in the outer disk region survive for > 4000 yr without showing inward migration, but we cannot determine whether these particles survive for a further long period. However, if these particles survive for a very long time, the dust grains will grow and may form planetesimals or protoplanets. Thus, this study suggests that the outer disk regions where dust grains accumulate without inward radial drift could be a favored place of planet formation. The number of dust particles calculated in this study is not large (102,984 particles, including gas test particles, for details, see Paper I), so it is difficult to quantitatively estimate the amount of dust grains orbiting in the outer disk region. The purpose of this study was to qualitatively investigate the dust motion in a growing disk during the main accretion phase and we do not extend the discussion to planet formation. Future studies will investigate long-term integration to determine the final fate of dust grains orbiting in the outer disk region.

ACKNOWLEDGEMENTS

We thank the referee for very useful comments and suggestions on this paper. We have benefited greatly from discussions with Yusuke Tsukamoto and Yoshihiro Kawasaki. This work was supported by the Japan Society for the Promotion of Science KAKENHI (JP17H06360, JP17K05387, JP17KK0096, JP21H00046, JP21K03617: MNM), JSPS KAKENHI grants (numbers JP20J12062), and NAOJ ALMA Scientific Research Grant Code 2022-22B. This research used the computational resources of the High-Performance Computing Infrastructure (HPCI) system provided by the CyberScience Center at Tohoku University, the Cybermedia Center at Osaka University, and the Earth Simulator at JAMSTEC through the HPCI System Research Project (project IDs hp200004, hp210004, hp220003). The simulations reported in this paper were also performed by 2021 and 2022 Koubo Kadai on the Earth Simulator (NEC SX-ACE and NEC SX-Aurora TSUBASA) at JAMSTEC.

DATA AVAILABILITY

The data underlying this article are available in the article and in its online supplementary material.

REFERENCES

- ALMA Partnership et al., 2015, *ApJ*, 808, L3
- Andrews S. M., 2020, *ARA&A*, 58, 483
- Andrews S. M., et al., 2018, *ApJ*, 869, L41
- Arakawa S., Matsumoto Y., Honda M., 2021, *ApJ*, 920, 27
- Aso Y., Machida M. N., 2020, *ApJ*, 905, 174
- Bae J., Isella A., Zhu Z., Martin R., Okuzumi S., Suriano S., 2022, arXiv e-prints, p. [arXiv:2210.13314](https://arxiv.org/abs/2210.13314)
- Banerjee R., Pudritz R. E., 2006, *ApJ*, 641, 949
- Bate M. R., 2022, *MNRAS*, 514, 2145
- Benisty M., et al., 2021, *ApJ*, 916, L2
- Blum J., Wurm G., 2008, *ARA&A*, 46, 21
- Galametz M., Maury A. J., Valdivia V., Testi L., Belloche A., André P., 2019, *A&A*, 632, A5
- Hayashi C., Nakazawa K., Nakagawa Y., 1985, in Black D. C., Matthews M. S., eds, *Protostars and Planets II*. pp 1100–1153
- Hennebelle P., Fromang S., 2008, *A&A*, 477, 9
- Hennebelle P., Commerçon B., Lee Y.-N., Chabrier G., 2020, *ApJ*, 904, 194
- Kawasaki Y., Koga S., Machida M. N., 2021, *MNRAS*, 504, 5588
- Kawasaki Y., Koga S., Machida M. N., 2022, *MNRAS*, 515, 2072
- Koga S., Tsukamoto Y., Okuzumi S., Machida M. N., 2019, *MNRAS*, 484, 2119
- Koga S., Kawasaki Y., Machida M. N., 2022, arXiv e-prints, p. [arXiv:2207.12907](https://arxiv.org/abs/2207.12907)
- Kwon W., Stephens I. W., Tobin J. J., Looney L. W., Li Z.-Y., van der Tak F. F. S., Crutcher R. M., 2019, *ApJ*, 879, 25
- Lebreuilly U., Commerçon B., Laibe G., 2020, *A&A*, 641, A112
- Lee Y.-N., Charnoz S., Hennebelle P., 2021, *A&A*, 648, A101
- Machida M. N., Hosokawa T., 2013, *MNRAS*, 431, 1719
- Machida M. N., Matsumoto T., 2011, *MNRAS*, 413, 2767
- Machida M. N., Tomisaka K., Matsumoto T., 2004, *MNRAS*, 348, L1
- Machida M. N., Matsumoto T., Hanawa T., Tomisaka K., 2006, *ApJ*, 645, 1227
- Machida M. N., Inutsuka S.-i., Matsumoto T., 2007, *ApJ*, 670, 1198
- Machida M. N., Inutsuka S.-i., Matsumoto T., 2009, *ApJ*, 699, L157
- Machida M. N., Inutsuka S.-i., Matsumoto T., 2014, *MNRAS*, 438, 2278
- Machida M. N., Matsumoto T., Inutsuka S.-i., 2016, *MNRAS*, 463, 4246
- Marchand P., Tomida K., Tanaka K. E. I., Commerçon B., Chabrier G., 2020, *ApJ*, 900, 180
- Marchand P., Guillet V., Lebreuilly U., Mac Low M. M., 2021, *A&A*, 649, A50
- Marchand P., Guillet V., Lebreuilly U., Mac Low M. M., 2022, *A&A*, 666, A27
- Mayor M., Queloz D., 1995, *Nature*, 378, 355
- Nakano T., Nishi R., Umebayashi T., 2002, *ApJ*, 573, 199
- Okuzumi S., Tanaka H., Kobayashi H., Wada K., 2012, *ApJ*, 752, 106
- Okuzumi S., Momose M., Sirono S.-i., Kobayashi H., Tanaka H., 2016, *ApJ*, 821, 82
- Ormel C. W., 2014, *ApJ*, 789, L18
- Ormel C. W., Cuzzi J. N., 2007, *A&A*, 466, 413
- Podio L., et al., 2020, *A&A*, 642, L7
- Sato T., Okuzumi S., Ida S., 2016, *A&A*, 589, A15
- Sheehan P. D., Tobin J. J., Federman S., Megeath S. T., Looney L. W., 2020, *ApJ*, 902, 141
- Shibaike Y., Mori S., 2022, arXiv e-prints, p. [arXiv:2211.08947](https://arxiv.org/abs/2211.08947)
- Takahashi S. Z., Muto T., 2018, *ApJ*, 865, 102
- Tokuda K., et al., 2020, *ApJ*, 899, 10

- Tomida K., Tomisaka K., Matsumoto T., Hori Y., Okuzumi S., Machida M. N., Saigo K., 2013, [ApJ](#), **763**, 6
- Tomida K., Machida M. N., Hosokawa T., Sakurai Y., Lin C. H., 2017, [ApJ](#), **835**, L11
- Tsukamoto Y., Iwasaki K., Okuzumi S., Machida M. N., Inutsuka S., 2015, [ApJ](#), **810**, L26
- Tsukamoto Y., Machida M. N., Susa H., Nomura H., Inutsuka S., 2020, [ApJ](#), **896**, 158
- Tsukamoto Y., Machida M. N., Inutsuka S., 2021a, [ApJ](#), **913**, 148
- Tsukamoto Y., Machida M. N., Inutsuka S.-i., 2021b, [ApJ](#), **920**, L35
- Tu Y., Li Z.-Y., Lam K. H., 2022, [MNRAS](#), **515**, 4780
- Tychoniec Ł., et al., 2020, [A&A](#), **640**, A19
- Valdivia V., Maury A., Brauer R., Hennebelle P., Galametz M., Guillet V., Reissl S., 2019, [MNRAS](#), **488**, 4897
- Wada K., Tanaka H., Okuzumi S., Kobayashi H., Suyama T., Kimura H., Yamamoto T., 2013, [A&A](#), **559**, A62
- Weidenschilling S. J., 1977, [MNRAS](#), **180**, 57
- Wurster J., Bate M. R., Price D. J., 2019, [MNRAS](#), **489**, 1719
- Xu W., Kunz M. W., 2021a, [MNRAS](#), **502**, 4911
- Xu W., Kunz M. W., 2021b, [MNRAS](#), **508**, 2142

This paper has been typeset from a $\text{\TeX}/\text{\LaTeX}$ file prepared by the author.